Gravitational-Wave Detector for Postmerger Neutron Stars

Zhang, Teng; Yang, Huan; Martynov, Denis; Schmidt, Patricia; Miao, Haixing

DOI:
10.1103/PhysRevX.13.021019

Document Version
Publisher's PDF, also known as Version of record

Citation for published version (Harvard):
Zhang, T, Yang, H, Martynov, D, Schmidt, P & Miao, H 2023, 'Gravitational-Wave Detector for Postmerger Neutron Stars: Beyond the Quantum Loss Limit of the Fabry-Perot-Michelson Interferometer', *Physical Review X*, vol. 13, no. 2, 021019. https://doi.org/10.1103/PhysRevX.13.021019

Gravitational-Wave Detector for Postmerger Neutron Stars: Beyond the Quantum Loss Limit of the Fabry-Perot-Michelson Interferometer

Teng Zhang,[1,2,3,*] Huan Yang,[4,5,†] Denis Martynov,[1] Patricia Schmidt,[1] and Haixing Miao[6,7,‡]

[1]School of Physics and Astronomy, and Institute for Gravitational Wave Astronomy, University of Birmingham, Edgbaston, Birmingham B15 2TT, United Kingdom
[2]Department of Gravitational Waves and Fundamental Physics, Maastricht University, 6200 MD Maastricht, Netherlands
[3]Nikhef, Science Park 105, 1098 XG Amsterdam, Netherlands
[4]Perimeter Institute for Theoretical Physics, Waterloo, Ontario N2L 2Y5, Canada
[5]University of Guelph, Guelph, Ontario N1G 2W1, Canada
[6]Department of Physics, Tsinghua University, Beijing 100084, China
[7]Frontier Science Center for Quantum Information, Beijing 100084, China

(Received 24 December 2022; revised 13 March 2023; accepted 7 April 2023; published 4 May 2023)

Advanced gravitational-wave detectors that have made groundbreaking discoveries are Michelson interferometers with resonating optical cavities as their arms. As light travels at a finite speed, these cavities are optimal for enhancing signals at frequencies within the bandwidth, beyond which, however, a small amount of optical loss will significantly impact the high-frequency signals. We find an elegant interferometer configuration with an "L resonator" as the core, significantly surpassing the loss-limited sensitivity of dual-recycled Fabry-Perot-Michelson interferometers at high frequencies. Following this concept, we provide a broadband design of a 25-km detector with outstanding sensitivity between 2 and 4 kHz. We perform Monte Carlo population studies of binary neutron-star mergers, given the most recent merger rate from the GWTC-3 catalog and several representative neutron-star equations of state. We find that the new interferometer configuration significantly outperforms other third-generation detectors by a factor of 1.7 to 4 in the signal-to-noise ratio of the postmerger signal. Assuming a detection threshold with signal-to-noise ratio > 5 and for the cases we explore, the new design is the only detector that robustly achieves a detection rate of the neutron-star postmerger larger than one per year, with the expected rate between $\mathcal{O}(1)$ and $\mathcal{O}(10)$ events per year.

DOI: 10.1103/PhysRevX.13.021019 Subject Areas: Astrophysics, Gravitation, Optics

I. INTRODUCTION

In 2015, the first direct detection of gravitational waves was made by the LIGO-Virgo Collaboration [1]. Since then, gravitational waves have become a new window for observing the Universe and probing the unexplored territories in astrophysics, cosmology, and fundamental physics. Until now, more than 90 compact-binary-merger events have been confidently observed by the network of advanced detectors, including Virgo and KAGRA [2]. Within these events, the detection of a binary neutron-star coalescence GW170817 [3] followed shortly by a short gamma-ray burst GRB 170817A [4], and the series of joint observations of electromagnetic counterparts [5] have had profound scientific impacts: This multimessenger discovery confirmed that binary neutron-star mergers are the origin of at least some short gamma-ray bursts and a production site for heavy elements via rapid neutron capture [5]. In the cosmology aspect, GW170817 has led to an independent measurement of the Hubble constant [6]. It also provided unique access to probe the internal structure of neutron stars and their equation of state by constraining their tidal deformability [3,7–11]. With both gravitational-wave and gamma-ray measurements, new constraints and bounds have been placed on the speed of gravitational waves and the violation of Lorentz invariance, in addition to a new test of the equivalence principle [4].

Current gravitational-wave detectors are only sensitive to the inspiral part of binary neutron-star mergers, as shown in the analysis of GW170817. The postmerger

*Corresponding author.
tzhang@star.sr.bham.ac.uk
†Corresponding author.
hyang@perimeterinstitute.ca
‡Corresponding author.
haixing@tsinghua.edu.cn

gravitational-wave signal, which concentrates in the kilohertz band, encodes essential information to answer many important questions, e.g., the origin(s) of heavy-element nucleosynthesis, the engine of gamma-ray jets, and the inner structure of the neutron star under extreme conditions. In particular, the merger and postmerger signals provide access to completely unexplored regimes in the quantum chromodynamics phase diagram beyond the reach of terrestrial collision experiment [12], where the novel phase of matter may appear, e.g., from hadron-quark phase transition [13–15].

The successful performance of current gravitational-wave detectors relies on their Michelson-type design. In addition to the canonical Michelson interferometer configuration, extra mirrors have been introduced in the arms to form Fabry-Perot cavities which boost both the optical power and the gravitational-wave signals, giving the so-called Fabry-Perot-Michelson (FPMI) interferometer [16]. With these modifications, the shot-noise-limited sensitivity is improved by orders of magnitude within the cavity bandwidth, typically from a few hertz to tens of hertz.

On the other hand, the binary neutron-star postmerger signals are mainly between 2 and 4 kHz, which is beyond the optimal band of current gravitational-wave detectors. To better explore neutron-star physics, there are various ideas developed to improve the high-frequency sensitivity of modern and future detectors based on the dual-recycled Fabry-Perot-Michelson (DRFPMI) interferometer, which includes a power recycling cavity at the bright port and a signal recycling cavity and signal extraction cavity (SEC) at the dark port to further enhance the arm cavity power and adjust the detector response [17,18]. One straightforward approach is to make use of the adjustability of the SEC, which forms a coupled system with the arm cavity. For example, the signal resonant frequency of the detector can be shifted to higher frequencies by constant SEC detuning [19] or exploring the SEC-arm coupled-cavity resonance [20–22]. More sophisticated quantum schemes, including the white-light cavity [23–28] and the nonlinear optical parametric amplifier [29–33], aim to broaden the effective bandwidth of the detector without sacrificing its peak sensitivity, hence overcoming the Mizuno limit [34]. However, it is the optical loss that sets a universal and ultimate sensitivity limit of a quantum detector [35]. The schemes mentioned above for improving the high-frequency sensitivity are all severely constrained by the optical losses in the SEC, which directly attenuate the signal emerging from the arm cavity. Even worse, the SEC loss-limited high-frequency sensitivity is independent of the arm length. Several studies have been carried out to explore various techniques to saturate or overcome the SEC loss limit [36,37]. It has been realized that a sloshing-type Sagnac configuration can beat the SEC loss limit by adding a filter cavity between two arms and thus shaping coupled-cavity resonances in the absence of a SEC. However, the filter cavity loss becomes the new limiting factor as another internal loss [37]. Physically, the intrinsic limit of high-frequency sensitivity comes from the decay of signal beyond the bandwidth of the single cavity where the signal is generated and circles around.

In order to surpass the loss limit of gravitational-wave detectors at high frequencies, the question becomes whether it is possible to resonate high-frequency signals in the arm cavity by itself. Meanwhile, the laser carrier needs to resonate to maintain the high power. It motivates the idea of taking advantage of resonance at free spectral range away from the carrier frequency [38]. However, the detector's response to gravitational waves essentially degrades around the free-spectral-range frequency [39–41]. For gravitational waves from the normal direction, the alteration in travel time for light cancels out if the duration of the round-trip matches the period of the gravitational wave.

In this paper, we provide an elegant detector scheme satisfying all criteria. The SEC loss-limited lower-bound sensitivity of the new detector can be orders of magnitude better than a DRFPMI interferometer at high frequencies. A conceptual design of the new detector, including all other losses, surpasses the quantum loss limit of currently proposed gravitational-wave detectors several times. In Sec. II, we introduce the principle of the core of the new detector, an "L resonator." In Sec. III, we present the complete interferometer and its quantum noise. In Sec. IV, we deliver the conceptual design of the new detector and model the noise budget. In Sec. V, we demonstrate the ability of the new detector to detect the postmerger signal of binary neutron-star coalescence and dark-matter-induced neutron-star collapse.

II. PRINCIPLE

To illustrate the principle of the new scheme, we start with the fundamental FPMI interferometer. Here, we define 2 orthogonal degrees of freedom of motion: the common "+" and differential "−" motions of end test masses (ETMs) in the x and y arms,

$$\Delta L_+ = \Delta L_x + \Delta L_y, \qquad \Delta L_- = \Delta L_y - \Delta L_x. \quad (1)$$

The differential mode signal transmits to the dark port, and the common mode signal appears at the bright port. The interferometer's responses to the sidebands of both modes are identical and proportional to

$$G_{\mathrm{FPMI},+/-} = \frac{\sqrt{2T_{\mathrm{ITM}}}}{|e^{2i\Omega\tau} - \sqrt{R_{\mathrm{ITM}}}|}, \quad (2)$$

where Ω is the angular frequency of sideband $\tau \equiv L/c$, L is the arm length, T_{ITM} and R_{ITM} are the transmissivity and reflectivity of the input test mass (ITM).

We propose an L resonator as shown in Fig. 1. Such a resonator responds to the two modes of motion in different manners, giving separated resonant frequencies. The phase variation of light after a round-trip in the cavity is $\Delta\phi(t) = (2\omega_0/c)[\Delta L_x(t-2\tau) + \Delta L_y(t)]$, which, in the frequency domain, can be written as

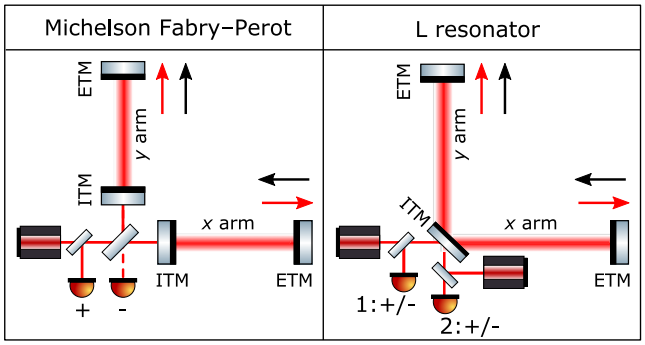

FIG. 1. Schematic of the FPMI interferometer and the L resonator. They are both sensitive to 2 degrees of freedom of motion: naming common + mode indicated by red arrows, and differential − mode (gravitational-wave mode) indicated by black arrows.

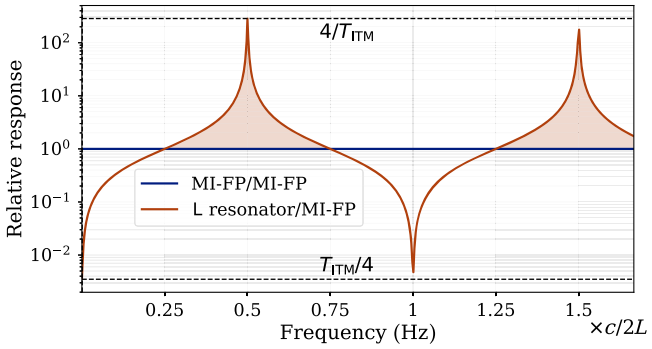

FIG. 2. The relative response of the L resonator and FPMI interferometer to the differential mode. The L resonator outperforms at $c/4L$ and $3c/4L$ with a relative amplification of $4/T_{\rm ITM}$, where $T_{\rm ITM}$ is chosen as 0.014. In contrast, the FPMI interferometer outperforms around frequency 0 Hz and $c/2L$.

$$\Delta\phi(\Omega) = \frac{2\omega_0}{c}(1 \pm e^{-2i\Omega\tau})\Delta L_{\pm}(\Omega), \tag{3}$$

where ω_0 is the angular frequency of the carrier. It is clear that when $\Omega/2\pi = Nc/2L$ (N is an integer), the phase shift of + mode reaches maximum; in contrast, the − mode peaks at $\Omega/2\pi = Nc/2L + c/4L$. Here we pump the resonator by two lasers from both input ports, which give balanced power in the two orthogonal arms [42]. The signal of both modes of motion will appear at both ports as indicated in Fig. 1. The responses of the two ports to the + and − mode are proportional to

$$G_{L,1,+} = G_{L,2,+} = \frac{\sqrt{T_{\rm ITM}}}{|e^{2i\Omega\tau} - \sqrt{R_{\rm ITM}}|},$$
$$G_{L,1,-} = -G_{L,2,-} = \frac{\sqrt{T_{\rm ITM}}}{|e^{2i\Omega\tau} + \sqrt{R_{\rm ITM}}|}. \tag{4}$$

By combining and splitting the + and − mode signals at two ports, we can tell the L resonator has an identical + mode response to the FPMI interferometer. Regarding the − mode, the L resonator has $4/T_{\rm ITM}$ times larger response at $c/4L$, as shown in Fig. 2. The expense is around $\Omega = 0$ and $c/2L$. It is worth noting that, at $\Omega = 0$, the response is not zero, as one may infer directly from Eq. (3).

How about its response to gravitational waves? Treating the ITM and ETM in the x arm or y arm of the L resonator as the boundary of the photon's trajectory in two directions, the round-trip phase in one direction under the projection of the gravitational waves is the same as in the Michelson interferometer where the beam splitter (BS) and ETM form the boundary. The fractional change of the travel time of light in one arm $D(\Omega, n_e)$ can be expressed by Eq. (5) in Ref. [41], where $n_e \equiv n_i e^i$. n_i is the traveling direction of gravitational plane wave, and e^i is the vector aligned to one arm. By calculating the optical field after traveling through the whole cavity, the cavity's response is proportional to $\sqrt{2}\omega_0\tau G_{L,1,-}D^{ij}$, where $D^{ij} = D(\Omega, n_k e_x^k)e_x^i e_x^j - D(\Omega, n_l e_x^l)e_y^i e_y^j$ is the detector tensor. It is the same as that of the Michelson interferometer [39–41,44]. The antenna response for each polarization is $F_{+,\times} = D_{ij}\epsilon^{ij}_{+,\times}$, where $\epsilon^{ij}_{+,\times}$ is the polarization tensor for the + and × polarizations [41,45], respectively. In the special case, the strain of the normal incident waves can be mapped to an equivalent differential displacement as follows:

$$\Delta L_-(\Omega) = L\frac{\sin\Omega\tau}{\Omega\tau}h(\Omega). \tag{5}$$

It is clear that only at multiples of $c/2L$, instead of $c/4L$, the gravitational wave corresponds to 0 effective displacements. In later sections, the strain sensitivities are shown by including the antenna response $\sqrt{|F_+|^2 + |F_\times|^2}$ for gravitational waves traveling at an angle of 15° with respect to the normal direction.

III. THE COMPLETE INTERFEROMETER AND QUANTUM NOISE

Each output port of the L resonator is sensitive to both common and differential modes. We can decouple the two modes of signals through an electronic system after measuring their signals. More practically, we can use a single laser and add a BS to form the complete interferometer as shown in Fig. 3, which decouples the two modes spatially. In Fig. 3, the sideband extraction mirror (SEM) and power recycling mirror (PRM) are also included. Note that in the lossless case, the laser travels in and returns along the same input port, and the reflection port turns out to be dark. Therefore, the BS behaves more like the one in the Michelson instead of the Sagnac interferometer, as the topology might indicate. The SEM helps decrease the sidebands' storage time around $c/4L$, therefore broadening the detector bandwidth [34]. In contrast, it increases the low-frequency sideband storage time, which refers to the signal recycling scheme in the DRFPMI interferometer [17,34]. A similar high-frequency resonance can be

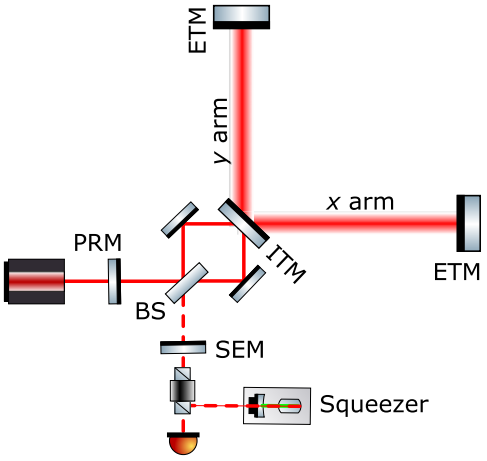

FIG. 3. The schematic of the new interferometer comprised of the L resonator and a central Michelson interferometer. It also includes a power recycling mirror (PRM) and signal extraction mirror (SEM). Constant phase squeezing is injected from the dark port.

achieved by the synchronous interferometer [46–50], which uses a ring cavity as its core. It realizes a speed-type measurement that suppresses the signals at low frequencies. The new interferometer is a position meter sensitive to signals toward dc.

The quantum noise of the new interferometer can be derived following the conventional approach of modeling the field propagation in the interferometer. The single-sided quantum-noise power spectral density of the interferometer in the unit of m^2/Hz is

$$S(\Omega)=\frac{c^2\hbar|e^{2i\Omega\tau}+\sqrt{R_{\rm SEC}}|^2}{4\omega_0 P_{\rm arm}T_{\rm SEC}}+\frac{16\hbar\omega_0 P_{\rm arm}T_{\rm SEC}}{c^2M^2|e^{2i\Omega\tau}+\sqrt{R_{\rm SEC}}|^2\Omega^4}, \tag{6}$$

where M is the mass of each ETM. Here, $T_{\rm SEC}$ and $R_{\rm SEC}$ are the effective transmissivity and reflectivity of the SEC formed by the ITM and SEM:

$$T_{\rm SEM}\equiv\frac{T_{\rm ITM}T_{\rm SEM}}{[1-\sqrt{R_{\rm ITM}R_{\rm SEM}}]^2}, \tag{7}$$

where $T_{\rm SEM}, R_{\rm SEM}$ are the power transmissivity and reflectivity of SEM. More precisely, we include the additional phase gained by the sidebands propagating in the SEC. There is

$$S(\Omega)=\frac{c^2\hbar|\mathcal{C}|^2}{4\omega_0 P_{\rm arm}T_{\rm ITM}T_{\rm SEM}}+\frac{16\hbar\omega_0 P_{\rm arm}T_{\rm ITM}T_{\rm SEM}}{c^2M^2|\mathcal{C}|^2\Omega^4}, \tag{8}$$

where

$$\mathcal{C}=e^{2i\Omega(\tau+\tau_s)}+\sqrt{R_{\rm ITM}}\left[e^{2i\Omega\tau_s}-e^{2i\Omega\tau}\sqrt{R_{\rm SEM}}\right]-R_{\rm SEM}. \tag{9}$$

Here $\tau_s\equiv L_{\rm SEC}/c$, $L_{\rm SEC}$ is the SEC length. The first term of Eq. (8) is the shot noise $S_{\rm shot}$, and the second term denotes the radiation-pressure noise. The power spectral density of the SEC loss can be calculated as

$$S_{\rm SEC}(\Omega)=\epsilon_{\rm SEC}\left[\frac{c^2\hbar|e^{2i\Omega\tau}+\sqrt{R_{\rm ITM}}|^2}{4\omega_0 P_{\rm arm}T_{\rm ITM}}+\frac{16\hbar\omega_0 P_{\rm arm}T_{\rm ITM}}{c^2M^2|\mathcal{C}|^2\Omega^4}\right], \tag{10}$$

where $\epsilon_{\rm SEC}$ is the SEC loss coefficient. The power spectral density of the input loss is $S_{\rm in}(\Omega)=\epsilon_{\rm in}S(\Omega)$, where $\epsilon_{\rm in}$ is the input loss coefficient. The power spectral density of the output loss is $S_{\rm out}(\Omega)=\epsilon_{\rm out}S_{\rm shot}(\Omega)/(1-\epsilon_{\rm out})$, where $\epsilon_{\rm out}$ is the output loss coefficient. The arm loss power spectral density can be calculated as

$$S_{\rm arm}(\Omega)=\epsilon_{\rm arm}\left[\frac{c^2\hbar}{8\omega_0 P_{\rm arm}}+\frac{8\hbar\omega_0 P_{\rm arm}|e^{2i\Omega\tau_s}-\sqrt{R_{\rm ITM}R_{\rm SEM}}|^2}{c^2M^2|\mathcal{C}|^2\Omega^4}\right], \tag{11}$$

where $\epsilon_{\rm arm}$ is the arm loss coefficient.

IV. CONCEPTUAL DESIGN AND NOISE BUDGET

Targeting the postmerger signals of binary neutron stars, typically between 2 and 4 kHz, we propose a detector with each arm length 25 km, which results in peak sensitivity at 3 kHz. The sensitivities of the new detector, Advanced LIGO+ (A+) [51,52], and other third-generation detectors—Neutron Star Extreme Matter Observatory (NEMO) [21] Einstein Telescope (ET) [53], and Cosmic Explorer (CE) [54,55]—are compared in Fig. 4.

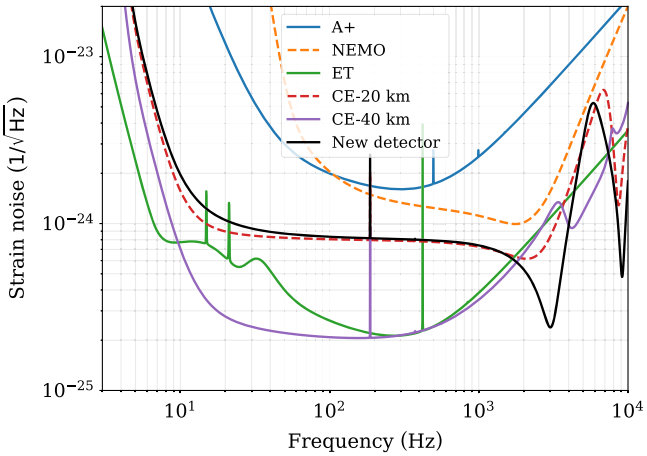

FIG. 4. Strain sensitivity of the 25-km new detector in comparison to A+ [51,52], NEMO [21], ET [53], the "postmerger" tuned CE-20-km and the CE-40-km [54,55] detectors. The sensitivity of ET corresponds to the combined three 10-km triangular configurations. The new detector gives superior sensitivity in the frequency range of 2–4 and 8–10 kHz. The parameters of the new detector are listed in Table. I.

A. Interferometer design

In such a detector, we choose a laser wavelength at 1064 nm and fused silica as the mirror material, the same as in the LIGO and Virgo detectors [51,56]. We target the arm cavity power 1.5 MW, which can be obtained with a 165-W input laser and 100-ppm round-trip arm cavity loss (equivalent to 50-ppm loss in each arm cavity of the DRFPMI interferometer). On the conceptual level, we reasonably assume other power degradation mechanisms, e.g., the point absorbers on the surface of optics [57], the parametric acousto-optic coupling [58] will be manageable in the future benefiting from both optimizing the detector's technical design and technology research and development. The ITM transmissivity is chosen as 0.014. The SEM transmissivity is chosen as 0.06, and the SEC length is chosen as 50 m. The resulting detector half-bandwidth is approximately 300 Hz.

The radius of curvature of two ETMs is chosen to be 40 km (cavity g factor approximately 0.06), resulting in a beam size of 13.2 cm on the ETMs. The beam is elliptical on the ITM, with sizes of 8 and 11.3 cm in two axes (11.3 cm $= \sqrt{2} \times 8$ cm, where 8 cm is the waist size). We adopt the mirror radius and thickness of 34 and 40 cm, respectively, giving total weight of approximately 320 kg. In the new detector, the ITM's displacement along its normal is of the + mode. Ideally, the gravitational wave channel will not be affected by the larger thermal fluctuations of the ITM resulting from its suboptimal geometry [59]. We choose the ITM radius of 34 cm and thickness 17 cm giving a mirror mass of 136 kg. The coating material of the ITM should have low optical absorption to reduce the heat load, hence reducing the optical loss in the recycling cavity from the thermal distortion [60]. However, it is not required to have a low mechanical loss, which is necessary to have by the ITMs in the DRFPMI interferometer.

B. Radiation-pressure noise and squeezing

In the new detector, only two ETMs contribute to the effective differential mode, which is half reduced compared with the DRMIFP interferometer. Equivalently, the reduced mirror mass of the differential mode is a factor of 2 larger; hence, the quantum-radiation-pressure amplitude noise is reduced by a factor of 2. It is straightforward to read that Eq. (8) reaches the minimum value when the shot noise and the radiation-pressure noise are equal:

$$S(\Omega) \geq \frac{4\hbar}{M\Omega^2}, \tag{12}$$

which is the power spectral density of the standard quantum limit of the new interferometer. It is only half the standard quantum limit of a DRMIFP interferometer [61].

Benefiting from the naturally reduced radiation-pressure noise, we adopt only constant phase squeezing instead of frequency-dependent squeezing. As a result, the usual kilometer-long filter cavity is not required. We assume 18-dB constant phase squeezing can be generated. The loss projection on the input path is 1.5%, including 1% from the optical parametric amplifier and 0.5% from the Faraday isolator. Note that the input loss budget is less than the estimation in other third-generation detectors, where a filter cavity is required on the input chain. It will result in 15-dB squeezing into the interferometer and give 15-dB amplification of radiation-pressure noise. The output path, including the Faraday isolator (0.5%), output mode cleaner (2%), and the photodiodes (1%), contribute a total 3.5% loss [62]. Including the internal loss from the SEC (500 ppm) and arm cavity (100 ppm), (10–11.5)-dB squeezed shot noise is observed over the whole frequency band, with 11.5-dB squeezing at the peak sensitivity. The detailed quantum-noise compositions are shown in Fig. 5.

C. Arm cavity noise

The arm cavity effective mirror displacement noises are reduced compared with the equivalent DRFPMI interferometer, again benefiting from the insusceptibility to ITM motions.

We model the noise budget of the new detector using the software PYGWINC [63]. The noise modeling is based on the CE-40-km design [64]. For the coating thermal Brownian noise modeling, we assume a factor 4 improvement from the mechanical loss of Ta_2O_5 and SiO_2 bilayer coatings, which is also the goal of A+ [52]. The ETM suspension design is assumed to be the quadruple pendulum suspension used in LIGO [64,65]. The vertical seismic and suspension thermal noise has the least coupling due to the finite radius of the curvature of Earth and is independent of the arm length in the unit of strain. They scale down by

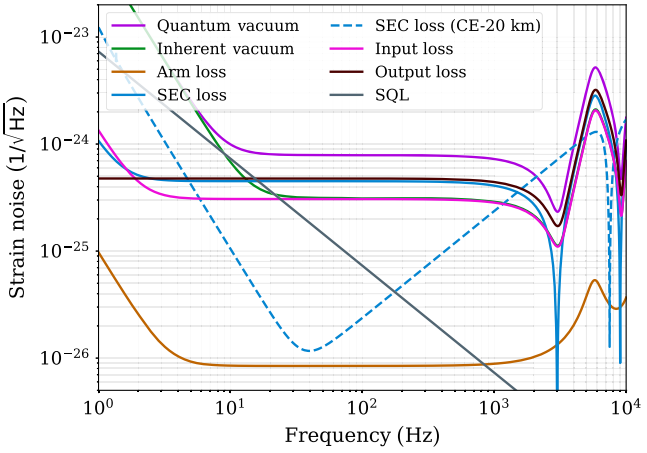

FIG. 5. Detailed quantum-noise budget of the new detector (solid lines). The SEC loss limit of the postmerger tuned CE-20-km detector (dashed line) is included for comparison. At 3 kHz, the SEC loss limit of the new detector is orders of magnitude lower than that of the postmerger tuned CE-20-km detector. The output loss limits the quantum noise of the new detector.

TABLE I. Parameters of the 25-km new detector.

Wavelength	1064 nm
Arm length	25 km
SEC length	50 m
Input laser power	165 W
Power recycling cavity power	10.6 kW
Arm circulating power	1.5 MW
ITM transmissivity	0.014
SRM transmissivity	0.06
Arm loss	100 ppm
SEC loss	500 ppm
Input loss	1.5%
Output loss	3.5%
Input squeezing level	18 dB
Result squeezing (shot noise)	10–11.5 dB
Result squeezing (radiation-pressure noise)	−15 dB
Substrate material	Silica
ITM and ETM mass	136 and 320 kg
ITM radius and thickness	34 and 17 cm
ETM radius and thickness	34 and 40 cm
ITM and ETM RoC	∞ and 40 km
ITM and ETM beam size	8 and 13.2 cm
BS radius and thickness	34 and 17 cm
BS beam size	8 cm
Coating loss angle (ETM and steering mirror)	9e-5 and 1.25e-5

$\sqrt{2}$ from CE-40 km. The horizontal seismic and suspension thermal noise increases by 1.13 $(40/25/\sqrt{2})$. Newtonian noise is also around a factor of 1.13 times the CE-40-km noise. The residual gas noise caused by the stochastic disturbance of molecular species onto the laser's phase [66] is not mirror displacement noise and will almost scale up by 1.6 (40/25). The gas damping noise, however, from the impinging of the gas particles onto test masses [67,68] scales up by 1.13.

D. Central Michelson noise

Different from the DRFPMI interferometer, where the arm cavity buildup factor attenuates the central Michelson noise, the optical path's fluctuations in the central Michelson noise of the new detector are non-negligible at low frequency and around $c/2L$ due to the antiresonance of the arm cavity in those frequency bands. The power spectral density of the Michelson differential noise can be mapped to the equivalent ETM noise as

$$S_{\mathrm{ETM}}(\Omega) = S_{\mathrm{Mi}}(\Omega)\frac{|e^{2i\Omega\tau} + \sqrt{R_{\mathrm{ITM}}}|^2}{4}, \qquad (13)$$

where $S_{\mathrm{Mi}}(\Omega)$ is the central Michelson noise and $S_{\mathrm{ETM}}(\Omega)$ is thus the detection noise. Such a fundamental noise can largely come from the change of the refractive index of the BS and ITM substrate due to inhomogeneous temperature fluctuations, so called substrate thermorefractive noise [69–71]. The central Michelson thermorefractive noise from both the BS and ITM substrates can be calculated by Eq. (2) in Ref. [70], including elliptical beam corrections. The beam size on the BS will be almost the same as on the ITM. We choose the BS geometry to be the same as the ITM with a radius 34 cm and a thickness 17 cm.

We also include the suspension, coating, and substrate thermal noise from the BS and the two steering mirrors between the BS and the ITM. The folding mirror gives coherent mirror displacement noise twice in a round-trip. It also introduces larger mirror thermal noise in each bounce than a straight reflection due to the interference fringe pattern [72,73]. It is a 50% addition in the power spectral density for coating Brownian noise [72,73], the dominated thermal noise. The steering mirror coatings have the same mechanical loss as the ETMs. For the seismic noise and seismic Newtonian noise of the central Michelson interferometer, the scale of the central Michelson interferometer should be smaller than the wavelength of the seismic waves; the motions of the Michelson mirrors can be largely coherent as a certain mix of differential and common modes. For simplicity, we assume uncorrelated noise from each mirror. The seismic isolation systems of central Michelson mirrors are the same as those of the ETMs. The detailed noise budget of the new detector is shown in Fig. 6.

As shown in Fig. 4, the sensitivity of the new detector is comparable to that of the postmerger tuned CE-20 km in the hundreds of hertz range. It starts to have better sensitivity from 1.5 kHz and shows more than a factor of 2 improvement in the frequency range from 2.6 to 3.8 kHz with the maximal improvement of 3.5 times occurring at 3 kHz.

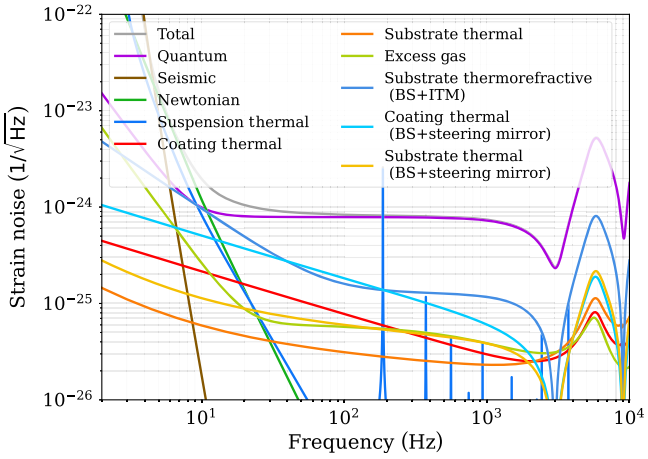

FIG. 6. Noise budget of the 25-km new detector. Above 20 Hz, the sensitivity of the new detector is limited by quantum shot noise. Instead of frequency-dependent squeezing, only constant phase squeezing is applied. The seismic noise. Newtonian noise and suspension thermal noise include both arm cavity and central Michelson noise. We present the BS and ITM coating and substrate noise separately. The noise budget is modeled by the software PYGWINC [63].

V. SCIENCE CASES

The new configuration leads to a broadband sensitivity as shown in Fig. 4; hence, such a detector will still be able to probe the astrophysics of compact binaries and cosmology similar to third-generation detectors (see, e.g., Ref. [74]), though with modified signal-to-noise ratios (SNRs). In this section, we highlight two specific science cases that become accessible due to the unparalleled sensitivity at high frequencies offered by the new design.

A. Neutron-star postmerger

The primary science target of this new detector design is the postmerger gravitational-wave signal of coalescing binary neutron-star systems. While the ringdown spectroscopy of binary black-hole coalescences provides a novel platform for tests of general relativity [75–78], the postmerger spectroscopy of binary neutron stars will likely shed light on our understanding of the equation of state of nuclear matter at high temperatures, complicated magneto-hydrodynamical processes involving neutrino generation and transport, novel phase(s) of nuclear matter, and the underlying mechanism of short gamma-ray bursts [79–87].

The postmerger waveform of binary neutron stars is a complicated (and unknown) function of the neutron-star masses, spins, and the equation of state. We perform an analysis similar to the one presented in Ref. [20] and choose five representative equations of state: TM1 [88], DD2 [89], SFHo [90], SLy [91], and APR4 [92] to cover a range of different stiffness. The neutron-star binary is assumed to be $1.35M_\odot + 1.35M_\odot$, and the corresponding waveforms are adopted from Refs. [93–96]. In Fig. 7, we present the waveforms of a source in different equations of state at a distance of 100 Mpc. Notice that the actual

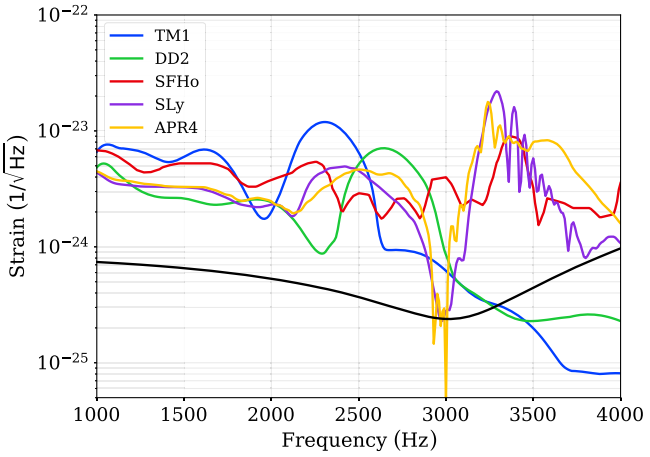

FIG. 7. The postmerger waveform of binary neutron stars in various of equations of state with peak mode frequency ranging from 2 to 4 kHz. The source distance is assumed to be 100 Mpc. Each neutron star in the binary is assumed to have equal mass $1.35M_\odot$. The black solid line represents the sensitivity of the new detector.

postmerger waveform depends on the remnant mass, spin, magnetic field level, and possibly many other factors, in addition to the equation of state. The goal of this new detector is to provide superior sensitivity covering from over 1 to 4 kHz, where most postmerger spectra belong. However, it is not necessary that the detector sensitivity is optimal for a particular waveform considering the uncertainty.

We assume the updated binary neutron-star merger rate after the third observing run of the Advanced LIGO-Virgo detector network, $105.5^{+190.2}_{-83.9}\ \mathrm{Gpc^{-3}\,yr^{-1}}$ [97]. We note that it is an order of magnitude smaller than the initial rate estimated after the detection of GW170817 [3] (and used in Ref. [20]). For each of the three equations of state, we apply Monte Carlo simulations to randomly sample binary neutron stars in their sky locations, inclinations, and distances according to the merger rate, assuming one year of observation time and a uniform distribution of binaries in comoving volume. We repeat this exercise 100 times to generate 100 universes with the same underlying distribution but different statistical realizations. We compute the postmerger SNR for each event, defined as

$$\mathrm{SNR} := 2\sqrt{\int_{f_{\mathrm{contact}}}^{4\ \mathrm{kHz}} df\,\frac{|\tilde{h}(f)|^2}{S_n(f)}}, \tag{14}$$

where $\tilde{h}$ is the frequency-domain postmerger waveform, $S_n(f)$ is the single-sided noise power spectral density of the considered detector, and f_{contact} is the frequency at which neutron stars collide with each other [93,98], which depends on the equation of state. It can be computed from the mass ratio of the binary and the compactness of the neutron stars [98]. The upper cutoff frequency is chosen to be 4 kHz to cover most of the spectral power of the postmerger waveform. We note that this is a slightly different definition of the postmerger SNR from the one used in Refs. [55,99], where instead of f_{contact} a fixed lower cutoff frequency of 1 kHz is used. Here we choose the equation-of-state-dependent contact frequency as we are not considering the part of the postmerger spectrum that overlaps with inspiral frequencies. The resulting median number of events with a postmerger SNR > 5 and the median SNR of the loudest event, averaged over the 100 realizations and assuming three different merger rates, are shown in Fig. 8. We find that the new design significantly outperforms—by a factor of 1.7 to 4—other third-generation detectors in detecting the postmerger signal of colliding neutron stars. If the detection threshold is chosen to be a SNR > 5, then only the new design is confidently expected to observe at least one event per year, whereas the detection rates for NEMO, ET, and CE are 1 to 2 orders of magnitude smaller for most of the equations of state. Notice that here the SNR is defined for the total postmerger waveform, which is greater than the SNR stemming from the excitation of individual oscillation

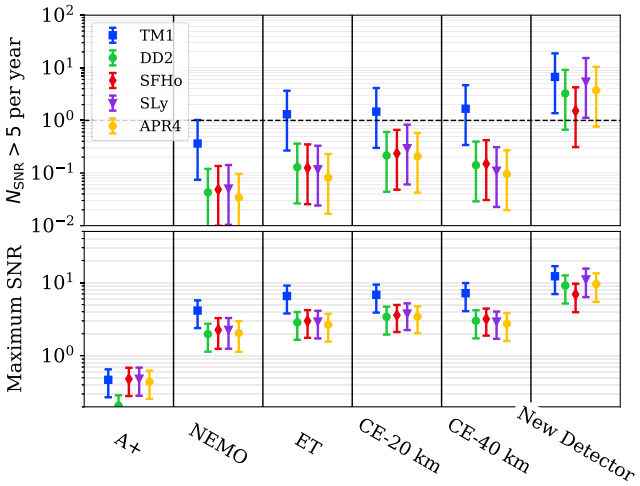

FIG. 8. Number of events with SNR greater than 5 (top) and the SNR of the loudest event (bottom), both are assuming one year of observing time. They are obtained from the median values in the Monte Carlo simulations. The upper ends of the error bars correspond to the case with the merger rate being 295.7 $\mathrm{Gpc}^{-3}\,\mathrm{yr}^{-1}$, the lower ends correspond to 21.6 $\mathrm{Gpc}^{-3}\,\mathrm{yr}^{-1}$, and the symbols correspond to 105.5 $\mathrm{Gpc}^{-3}\,\mathrm{yr}^{-1}$.

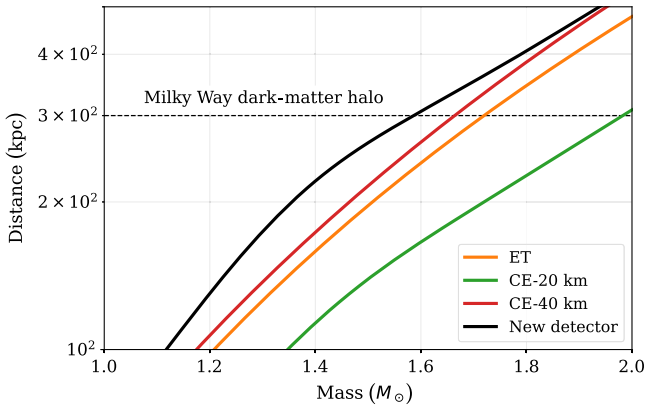

FIG. 9. Horizon distance for detecting the dark-matter-induced neutron-star collapse signal with different detector sensitivities, assuming the threshold SNR is 5.

modes of the postmerger object. Therefore, the new design provides the most promising platform to perform postmerger spectroscopy, i.e., resolving the "peak mode" and other secondary oscillation modes of the remnant [100].

B. Dark-matter-induced neutron-star collapse

In addition to the prominent sensitivity between 2 and 4 kHz, the new detector also has better sensitivity between 8 and 10 kHz. This section studies its potential advantage for an even higher-frequency science case.

It has been proposed that fermionic dark-matter particles may accumulate at the center of neutron stars and eventually collapse into a mini-black-hole because of the dissipative interaction. The neutron-star matter subsequently accretes onto the mini-black-hole in millisecond timescale and produces gravitational-wave emission in the kilohertz range, depending on the mass of the collapsing neutron star.

The primary gravitational-wave signal for a rotating neutron star is the 20 mode of the axisymmetric collapse. The collapse waveform in discussed in Ref. [101], which displays similar magnitude (in ψ_4) as the collapse waveform of the hypermassive neutron star as used in Ref. [38]. For simplicity, we use the phenomenological waveform model in Ref. [38] to compute the signal-to-noise ratio of these events:

$$h = A\frac{50\ \mathrm{Mpc}}{d}\sin(2\pi f t)e^{-\pi f|t|/Q} \tag{15}$$

with the prepeak part contributing a comparable SNR to the postpeak part. Here the mode frequency is inversely proportional to mass $f \sim 4.7\ \mathrm{kHz} \times (2.7M_\odot/M_{\mathrm{NS}})$, the quality factor is $Q \sim 2.5$, and the amplitude is estimated as $A \sim 0.8 \times 10^{-23}(4.7\ \mathrm{kHz}/f)^2$ (assuming the "TM1" equation of state). Notice that these values are expected to change for different neutron-star spin and equations of state. For example, the amplitude may change by at least a factor of 3 according to the equations of state used in Ref. [101], and the variation of frequency and quality factor may be $\lesssim 30\%$ or $\lesssim 20\%$, respectively [38].

As shown in Fig. 9, with the waveform model of the collapse process, we can estimate the horizon distance if the detection threshold is set to be a SNR $= 5$. The new design shows approximately 30% improvements in horizon distance for neutron-star mass around 1.4 solar mass compared with other third-generation detectors, benefiting from the secondary dip in the sensitivity curve of the new detector in Fig. 4. The enhanced horizon distance is reaching toward the edge of Milky Way's dark-matter halo for low-mass collapse events.

VI. CONCLUSION

As an extraordinary laboratory to study nuclear physics, the postmerger neutron stars call the demand to enhance the gravitational-wave detectors' sensitivity in the kilohertz band. The currently existing and proposed gravitational-wave detectors are based on the DRFPMI interferometer. Since the Fabry-Perot cavity is limited to having a narrow bandwidth to maintain its high-finesse operation, such configurations have suboptimal performance toward high frequencies. The fundamental limit from optical losses sets the barrier, particularly the loss in the SEC, which mixes with decayed high-frequency signals from the arm cavity.

In this work, we present an elegant interferometer based on an L-shaped optical resonator, which amplifies both the high-frequency gravitational-wave signals and carrier. The SEC loss-limited sensitivity of such an interferometer surpasses that of a DRFPMI interferometer by orders of

magnitude at high frequencies, more precisely, $4/T_{\mathrm{ITM}}$ at $c/4L$. Beyond its high-frequency superiority, its insusceptibility to ITM motions provides a factor of $\sqrt{2}$ suppression of displacement noises from the arm cavity mirrors and a factor of 2 suppression of the quantum-radiation-pressure noise. It also brings other advantages; for example, the constant phase squeezing turns out to be sufficient and the ITM coatings require us only to satisfy low optical absorption without demanding low mechanical loss. The drawback of the new interferometer is at low frequencies around 0 Hz where the noises in the central Michelson interferometer couple to the detector readout with the same gain of arm cavity noise. On the technical level, the potential technical topics, e.g., the parametric instability [58], radiation-pressure-induced angular instability of the arm cavity [102], and the required thermal compensation system [60] that will be different from the DRFPMI interferometer require a separate study in the future.

We apply the sensitivity of the new detector to measure its ability to detect the binary neutron-star postmergers through the Monte Carlo population simulation. Based on the chosen equations of state, the new detector has SNRs a factor of 1.7 to 4 of the other third-generation detectors. Taking the SNR > 5 as the threshold and given the merger rate ranging from 21.6 to 295.7 $\mathrm{Gpc}^{-3}\,\mathrm{yr}^{-1}$ according to the GWTC-3 catalog, the new detector can enable a maximal detection rate up to approximately 20 per year.

In addition, we explore the potential advantage of the new detector in its ability to detect dark-matter-induced neutron-star collapse. Benefiting from the conspicuous sensitivity between 8 and 10 kHz, which results from the second resonance of the new interferometer at $3c/4L$, it gives approximately 30% improvement for neutron stars with around 1.4 solar mass, in comparison to the horizon reach of other configurations.

ACKNOWLEDGMENTS

We thank the LVK Collaboration, Kevin Kuns, Daniel Brown, Mikhail Korobko, Jennifer Wright, Stefan Danilishin, Stefan Hild, and Sebastian Steinlechner for fruitful discussions. T. Z., D. M., P. S., and H. M. acknowledge the support of the Institute for Gravitational Wave Astronomy at the University of Birmingham, STFC Quantum Technology for Fundamental Physics scheme (Grant No. ST/T006609/1), and EPSRC New Horizon Scheme (Grant No. EP/V048872/1). T. Z. acknowledges the support of the Department of Gravitational Waves and Fundamental Physics in Maastricht University and E-TEST project. H. M. is supported by State Key Laboratory of Low Dimensional Quantum Physics and the start-up fund from Tsinghua University. D. M. is supported by the 2021 Philip Leverhulme grant. H. Y. is supported by the Natural Sciences and Engineering Research Council of Canada and in part by Perimeter Institute for Theoretical Physics. Research at Perimeter Institute is supported in part by the Government of Canada through the Department of Innovation, Science and Economic Development Canada and by the Province of Ontario through the Ministry of Colleges and Universities. P. S. acknowledges support from STFC Grant No. ST/V005677/1.

[1] B. P. Abbott *et al.* (LIGO Scientific Collaboration and Virgo Collaboration), *Observation of Gravitational Waves from a Binary Black Hole Merger*, Phys. Rev. Lett. **116**, 061102 (2016).

[2] R. Abbott *et al.* (LIGO Scientific Collaboration, Virgo Collaboration, and KAGRA Collaboration), *GWTC-3: Compact Binary Coalescences Observed by LIGO and Virgo during the Second Part of the Third Observing Run*, arXiv:2111.03606.

[3] B. P. Abbott, R. Abbott, T. D. Abbott *et al.* (LIGO Scientific Collaboration and Virgo Collaboration), *GW170817: Observation of Gravitational Waves from a Binary Neutron Star Inspiral*, Phys. Rev. Lett. **119**, 161101 (2017).

[4] B. P. Abbott, R. Abbott, T. D. Abbott, F. Acernese, K. Ackley, C. Adams, T. Adams, P. Addesso, R. X. Adhikari, V. B. Adya *et al.*, *Gravitational Waves and Gamma-Rays from a Binary Neutron Star Merger: GW170817 and GRB 170817A*, Astrophys. J. Lett. **848**, L13 (2017).

[5] B. P. Abbott *et al.*, *Multi-Messenger Observations of a Binary Neutron Star Merger*, Astrophys. J. **848**, L12 (2017).

[6] LIGO Scientific Collaboration, Virgo Collaboration, 1M2H Collaboration, Dark Energy Camera GW-EM Collaboration, DES Collaboration, DLT40 Collaboration, Las Cumbres Observatory Collaboration, VINROUGE Collaboration, and MASTER Collaboration, *A Gravitational-Wave Standard Siren Measurement of the Hubble Constant*, Nature (London) **551**, 85 (2017).

[7] B. P. Abbott *et al.* (LIGO Scientific and Virgo Collaborations), *GW170817: Measurements of Neutron Star Radii and Equation of State*, Phys. Rev. Lett. **121**, 161101 (2018).

[8] B. P. Abbott *et al.* (LIGO Scientific and Virgo Collaborations), *Properties of the Binary Neutron Star Merger GW170817*, Phys. Rev. X **9**, 011001 (2019).

[9] B. P. Abbott *et al.* (LIGO Scientific and Virgo Collaborations), *Model Comparison from LIGO-Virgo Data on GW170817's Binary Components and Consequences for the Merger Remnant*, Classical Quantum Gravity **37**, 045006 (2020).

[10] K. Chatziioannou, *Neutron Star Tidal Deformability and Equation of State Constraints*, Gen. Relativ. Gravit. **52**, 109 (2020).

[11] Z. Pan, Z. Lyu, B. Bonga, N. Ortiz, and H. Yang, *Probing Crust Meltdown in Inspiraling Binary Neutron Stars*, Phys. Rev. Lett. **125**, 201102 (2020).

[12] C. Schmidt and S. Sharma, *The Phase Structure of QCD*, J. Phys. G **44**, 104002 (2017).

[13] N. Yasutake, T. Maruyama, and T. Tatsumi, *Hot Hadron-Quark Mixed Phase Including Hyperons*, Phys. Rev. D **80**, 123009 (2009).

[14] E. R. Most, L. J. Papenfort, V. Dexheimer, M. Hanauske, S. Schramm, H. Stöcker, and L. Rezzolla, *Signatures of*

Quark-Hadron Phase Transitions in General-Relativistic Neutron-Star Mergers, Phys. Rev. Lett. **122**, 061101 (2019).

[15] A. Bauswein, N.-U. F. Bastian, D. B. Blaschke, K. Chatziioannou, J. A. Clark, T. Fischer, and M. Oertel, *Identifying a First-Order Phase Transition in Neutron-Star Mergers through Gravitational Waves*, Phys. Rev. Lett. **122**, 061102 (2019).

[16] R. Drever, *Laser Interferometer Gravitational Radiation Detectors*, AIP Conf. Proc. **96**, 335 (1983).

[17] D. E. McClelland, *An Overview of Recycling in Laser Interferometric Gravitational Wave Detectors*, Aust. J. Phys. **48**, 953 (1995).

[18] A. Buonanno and Y. Chen, *Scaling Law in Signal Recycled Laser-Interferometer Gravitational-Wave Detectors*, Phys. Rev. D **67**, 062002 (2003).

[19] D. Ganapathy, L. McCuller, J. G. Rollins, E. D. Hall, L. Barsotti, and M. Evans, *Tuning Advanced LIGO to Kilohertz Signals from Neutron-Star Collisions*, Phys. Rev. D **103**, 022002 (2021).

[20] D. Martynov, H. Miao, H. Yang, F. H. Vivanco, E. Thrane, R. Smith, P. Lasky, W. E. East, R. Adhikari, A. Bauswein, A. Brooks, Y. Chen, T. Corbitt, A. Freise, H. Grote, Y. Levin, C. Zhao, and A. Vecchio, *Exploring the Sensitivity of Gravitational Wave Detectors to Neutron Star Physics*, Phys. Rev. D **99**, 102004 (2019).

[21] K. Ackley, V. B. Adya, P. Agrawal, P. Altin, G. Ashton, M. Bailes, E. Baltinas, A. Barbuio, D. Beniwal, C. Blair *et al.*, *Neutron Star Extreme Matter Observatory: A Kilohertz-Band Gravitational-Wave Detector in the Global Network*, Pub. Astron. Soc. Aust. **37**, e047 (2020).

[22] J. Eichholz, N. A. Holland, V. B. Adya, J. V. van Heijningen, R. L. Ward, B. J. J. Slagmolen, D. E. McClelland, and D. J. Ottaway, *Practical Test Mass and Suspension Configuration for a Cryogenic Kilohertz Gravitational Wave Detector*, Phys. Rev. D **102**, 122003 (2020).

[23] A. Wicht, K. Danzmann, M. Fleischhauer, M. Scully, G. Müller, and R. Rinkleff, *White-Light Cavities, Atomic Phase Coherence, and Gravitational Wave Detectors*, Opt. Commun. **134**, 431 (1997).

[24] M. Zhou, Z. Zhou, and S. M. Shahriar, *Quantum Noise Limits in White-Light-Cavity-Enhanced Gravitational Wave Detectors*, Phys. Rev. D **92**, 082002 (2015).

[25] H. Miao, Y. Ma, C. Zhao, and Y. Chen, *Enhancing the Bandwidth of Gravitational-Wave Detectors with Unstable Optomechanical Filters*, Phys. Rev. Lett. **115**, 211104 (2015).

[26] J. Bentley, P. Jones, D. Martynov, A. Freise, and H. Miao, *Converting the Signal-Recycling Cavity into an Unstable Optomechanical Filter to Enhance the Detection Bandwidth of Gravitational-Wave Detectors*, Phys. Rev. D **99**, 102001 (2019).

[27] M. A. Page, M. Goryachev, H. Miao, Y. Chen, Y. Ma, D. Mason, M. Rossi, C. D. Blair, L. Ju, D. G. Blair, A. Schliesser, M. E. Tobar, and C. Zhao, *Gravitational Wave Detectors with Broadband High Frequency Sensitivity*, Commun. Phys. **4**, 27 (2021).

[28] X. Li, J. Smetana, A. S. Ubhi, J. Bentley, Y. Chen, Y. Ma, H. Miao, and D. Martynov, *Enhancing Interferometer Sensitivity without Sacrificing Bandwidth and Stability: Beyond Single-Mode and Resolved-Sideband Approximation*, Phys. Rev. D **103**, 122001 (2021).

[29] M. Korobko, Y. Ma, Y. Chen, and R. Schnabel, *Quantum Expander for Gravitational-Wave Observatories*, Light Sci. Appl. **8**, 1 (2019).

[30] V. B. Adya, M. J. Yap, D. Töyrä, T. G. McRae, P. A. Altin, L. K. Sarre, M. Meijerink, N. Kijbunchoo, B. J. J. Slagmolen, R. L. Ward, and D. E. McClelland, *Quantum Enhanced kHz Gravitational Wave Detector with Internal Squeezing*, Classical Quantum Gravity **37**, 07LT02 (2020).

[31] J. W. Gardner, M. J. Yap, V. Adya, S. Chua, B. J. J. Slagmolen, and D. E. McClelland, *Nondegenerate Internal Squeezing: An All-Optical, Loss-Resistant Quantum Technique for Gravitational-Wave Detection*, Phys. Rev. D **106**, L041101 (2022).

[32] X. Li, M. Goryachev, Y. Ma, M. E. Tobar, C. Zhao, R. X. Adhikari, and Y. Chen, *Broadband Sensitivity Improvement via Coherent Quantum Feedback with PT Symmetry*, arXiv:2012.00836.

[33] C. Wang, C. Zhao, X. Li, E. Zhou, H. Miao, Y. Chen, and Y. Ma, *Boosting the Sensitivity of High-Frequency Gravitational Wave Detectors Using PT-Symmetry*, Phys. Rev. D **106**, 082002 (2022).

[34] J. Mizuno, K. Strain, P. Nelson, J. Chen, R. Schilling, A. Rüdiger, W. Winkler, and K. Danzmann, *Resonant Sideband Extraction: A New Configuration for Interferometric Gravitational Wave Detectors*, Phys. Lett. A **175**, 273 (1993).

[35] H. Miao, N. D. Smith, and M. Evans, *Quantum Limit for Laser Interferometric Gravitational-Wave Detectors from Optical Dissipation*, Phys. Rev. X **9**, 011053 (2019).

[36] T. Zhang, J. Bentley, and H. Miao, *A Broadband Signal Recycling Scheme for Approaching the Quantum Limit from Optical Losses*, Galaxies **9**, 3 (2021).

[37] T. Zhang, D. Martynov, H. Miao, and S. Danilishin, *Enhancing High Frequency Sensitivity of Gravitational Wave Detectors with a Sagnac Interferometer*, Phys. Rev. D **104**, 122003 (2021).

[38] T. Zhang, J. Smetana, Y. Chen, J. Bentley, D. Martynov, H. Miao, W. E. East, and H. Yang, *Toward Observing Neutron Star Collapse with Gravitational Wave Detectors*, Phys. Rev. D **103**, 044063 (2021).

[39] M. Rakhmanov, J. D. Romano, and J. T. Whelan, *High-Frequency Corrections to the Detector Response and Their Effect on Searches for Gravitational Waves*, Classical Quantum Gravity **25**, 184017 (2008).

[40] M. Rakhmanov, *On the Round-Trip Time for a Photon Propagating in the Field of a Plane Gravitational Wave*, Classical Quantum Gravity **26**, 155010 (2009).

[41] R. Essick, S. Vitale, and M. Evans, *Frequency-Dependent Responses in Third Generation Gravitational-Wave Detectors*, Phys. Rev. D **96**, 084004 (2017).

[42] If the resonator is pumped from one port, the power at the two ETMs will be imbalanced and cause a speed-meter response for the differential mode [43].

[43] M. Korobko, *Taming the Quantum Noise: How Quantum Metrology Can Expand the Reach of Gravitational-Wave Observatories*, Ph. D. thesis, Staats-und Universitätsbibliothek Hamburg Carl von Ossietzky, 2020, https://ediss2.sub.uni-hamburg.de/handle/ediss/8460.

[44] M. Maggiore, *Gravitational Waves: Volume 1: Theory and Experiments* (Oxford University Press, New York, 2007).
[45] W. G. Anderson, P. R. Brady, J. D. E. Creighton, and E. E. Flanagan, *Excess Power Statistic for Detection of Burst Sources of Gravitational Radiation*, Phys. Rev. D **63**, 042003 (2001).
[46] R. W. Drever, *Interferometric Detectors for Gravitational Radiation*, Lect. Notes Phys. **124**, 321 (1983), https://ui.adsabs.harvard.edu/abs/1983LNP...124..321D/abstract.
[47] J.-Y. Vinet, B. Meers, C. N. Man, and A. Brillet, *Optimization of Long-Baseline Optical Interferometers for Gravitational-Wave Detection*, Phys. Rev. D **38**, 433 (1988).
[48] B. J. Meers, *Recycling in Laser-Interferometric Gravitational-Wave Detectors*, Phys. Rev. D **38**, 2317 (1988).
[49] T. Akutsu, S. Kawamura, A. Nishizawa, K. Arai, K. Yamamoto, D. Tatsumi, S. Nagano, E. Nishida, T. Chiba, R. Takahashi, N. Sugiyama, M. Fukushima, T. Yamazaki, and M.-K. Fujimoto, *Search for a Stochastic Background of 100-MHz Gravitational Waves with Laser Interferometers*, Phys. Rev. Lett. **101**, 101101 (2008).
[50] A. Nishizawa, S. Kawamura, T. Akutsu, K. Arai, K. Yamamoto, D. Tatsumi, E. Nishida, M.-a. Sakagami, T. Chiba, R. Takahashi, and N. Sugiyama, *Laser-Interferometric Detectors for Gravitational Wave Backgrounds at 100 MHz: Detector Design and Sensitivity*, Phys. Rev. D **77**, 022002 (2008).
[51] J. Aasi, B. P. Abbott, R. Abbott, T. Abbott *et al.*, *Advanced LIGO*, Classical Quantum Gravity **32**, 074001 (2015).
[52] L. Barsotti, L. McCuller, M. Evans, and P. Fritschel, *The A+ Design Curve*, LIGO Report No. T1800042, 2018.
[53] S. Hild, M. Abernathy, F. Acernese, P. Amaro-Seoane, N. Andersson, K. Arun, F. Barone, B. Barr, M. Barsuglia, M. Beker, N. Beveridge, S. Birindelli, S. Bose, L. Bosi, S. Braccini, C. Bradaschia, T. Bulik, E. Calloni, G. Cella, E. C. Mottin *et al.*, *Sensitivity Studies for Third-Generation Gravitational Wave Observatories*, Classical Quantum Gravity **28**, 094013 (2011).
[54] M. Evans, R. X. Adhikari, C. Afle, S. W. Ballmer, S. Biscoveanu, S. Borhanian, D. A. Brown, Y. Chen, R. Eisenstein, A. Gruson *et al.*, *A Horizon Study for Cosmic Explorer: Science, Observatories, and Community*, arXiv:2109.09882.
[55] V. Srivastava, D. Davis, K. Kuns, P. Landry, S. Ballmer, M. Evans, E. D. Hall, J. Read, and B. S. Sathyaprakash, *Science-Driven Tunable Design of Cosmic Explorer Detectors*, Astrophys. J. **931**, 22 (2022).
[56] F. Acernese, M. Agathos, K. Agatsuma, D. Aisa, N. Allemandou, A. Allocca, J. Amarni, P. Astone *et al.*, *Advanced Virgo: a Second-Generation Interferometric Gravitational Wave Detector*, Classical Quantum Gravity **32**, 024001 (2014).
[57] A. F. Brooks, G. Vajente, H. Yamamoto, R. Abbott, C. Adams, R. X. Adhikari, A. Ananyeva, S. Appert, K. Arai, J. S. Areeda, Y. Asali, S. M. Aston, C. Austin, A. M. Baer, M. Ball, S. W. Ballmer, S. Banagiri, D. Barker, L. Barsotti, J. Bartlett *et al.*, *Point Absorbers in Advanced LIGO*, Appl. Opt. **60**, 4047 (2021).
[58] M. Evans, S. Gras, P. Fritschel, J. Miller, L. Barsotti, D. Martynov, A. Brooks, D. Coyne, R. Abbott, R. X. Adhikari, K. Arai, R. Bork, B. Kells, J. Rollins, N. Smith-Lefebvre, G. Vajente, H. Yamamoto, C. Adams, S. Aston, J. Betzweiser *et al.*, *Observation of Parametric Instability in Advanced LIGO*, Phys. Rev. Lett. **114**, 161102 (2015).
[59] Y. T. Liu and K. S. Thorne, *Thermoelastic Noise and Homogeneous Thermal Noise in Finite Sized Gravitational-Wave Test Masses*, Phys. Rev. D **62**, 122002 (2000).
[60] A. F. Brooks, B. Abbott, M. A. Arain, G. Ciani, A. Cole, G. Grabeel, E. Gustafson, C. Guido, M. Heintze, A. Heptonstall, M. Jacobson, W. Kim, E. King, A. Lynch, S. O'Connor, D. Ottaway, K. Mailand, G. Mueller, J. Munch, V. Sannibale *et al.*, *Overview of Advanced LIGO Adaptive Optics*, Appl. Opt. **55**, 8256 (2016).
[61] H. J. Kimble, Y. Levin, A. B. Matsko, K. S. Thorne, and S. P. Vyatchanin, *Conversion of Conventional Gravitational-Wave Interferometers into Quantum Nondemolition Interferometers by Modifying Their Input and/or Output Optics*, Phys. Rev. D **65**, 022002 (2001).
[62] M. Tse, H. Yu, N. Kijbunchoo, A. Fernandez-Galiana, P. Dupej, L. Barsotti, C. D. Blair, D. D. Brown, S. E. Dwyer, A. Effler, M. Evans, P. Fritschel, V. V. Frolov, A. C. Green, G. L. Mansell, F. Matichard, N. Mavalvala, D. E. McClelland, L. McCuller, T. McRae *et al.*, *Quantum-Enhanced Advanced LIGO Detectors in the Era of Gravitational-Wave Astronomy*, Phys. Rev. Lett. **123**, 231107 (2019).
[63] J. G. Rollins, E. Hall, C. Wipf, and L. McCuller, *PYGWINC: Gravitational Wave Interferometer Noise Calculator, Astrophysics Source Code Library* (2020).
[64] E. D. Hall, K. Kuns, J. R. Smith, Y. Bai, C. Wipf, S. Biscans, R. X. Adhikari, K. Arai, S. Ballmer, L. Barsotti, Y. Chen, M. Evans, P. Fritschel, J. Harms, B. Kamai, J. G. Rollins, D. Shoemaker, B. J. J. Slagmolen, R. Weiss, and H. Yamamoto, *Gravitational-Wave Physics with Cosmic Explorer: Limits to Low-Frequency Sensitivity*, Phys. Rev. D **103**, 122004 (2021).
[65] S. M. Aston, M. A. Barton, A. S. Bell, N. Beveridge, B. Bland, A. J. Brummitt, G. Cagnoli, C. A. Cantley, L. Carbone, A. V. Cumming, L. Cunningham, R. M. Cutler, R. J. S. Greenhalgh, G. D. Hammond, K. Haughian, T. M. Hayler, A. Heptonstall, J. Heefner, D. Hoyland *et al.*, *Update on Quadruple Suspension Design for Advanced LIGO*, Classical Quantum Gravity **29**, 235004 (2012).
[66] Z. Michael and S. Whitcomb, *Measurement of Optical Path Fluctuations Due to Residual Gas in the LIGO 40 Meter Interferometer*, LIGO Report No. P940008-x0, 1997, https://ui.adsabs.harvard.edu/abs/1996magr.meet.1434Z/abstract and https://dcc.ligo.org/LIGO-P940008/public.
[67] A. Cavalleri, G. Ciani, R. Dolesi, M. Hueller, D. Nicolodi, D. Tombolato, S. Vitale, P. Wass, and W. Weber, *Gas Damping Force Noise on a Macroscopic Test Body in an Infinite Gas Reservoir*, Phys. Lett. A **374**, 3365 (2010).
[68] R. Dolesi, M. Hueller, D. Nicolodi, D. Tombolato, S. Vitale, P. J. Wass, W. J. Weber, M. Evans, P. Fritschel, R. Weiss, J. H. Gundlach, C. A. Hagedorn, S. Schlamminger, G. Ciani, and A. Cavalleri, *Brownian Force Noise from Molecular Collisions and the Sensitivity of Advanced Gravitational Wave Observatories*, Phys. Rev. D **84**, 063007 (2011).

[69] V. Braginsky, M. Gorodetsky, and S. Vyatchanin, *Thermo-Refractive Noise in Gravitational Wave Antennae*, Phys. Lett. A **271**, 303 (2000).
[70] B. Benthem and Y. Levin, *Thermorefractive and Thermochemical Noise in the Beamsplitter of the GEO600 Gravitational-Wave Interferometer*, Phys. Rev. D **80**, 062004 (2009).
[71] *Optical Coatings and Thermal Noise in Precision Measurement*, edited by G. Harry, T. P. Bodiya, and R. DeSalvo (Cambridge University Press, Cambridge, England, 2012).
[72] D. Heinert, K. Craig, H. Grote, S. Hild, H. Lück, R. Nawrodt, D. A. Simakov, D. V. Vasilyev, S. P. Vyatchanin, and H. Wittel, *Thermal Noise of Folding Mirrors*, Phys. Rev. D **90**, 042001 (2014).
[73] J. R. Sanders and S. W. Ballmer, *Folding Gravitational-Wave Interferometers*, Classical Quantum Gravity **34**, 025003 (2016).
[74] M. Maggiore, C. V. D. Broeck, N. Bartolo, E. Belgacem, D. Bertacca, M. A. Bizouard, M. Branchesi, S. Clesse, S. Foffa, J. García-Bellido, S. Grimm, J. Harms, T. Hinderer, S. Matarrese, C. Palomba, M. Peloso, A. Ricciardone, and M. Sakellariadou, *Science Case for the Einstein Telescope*, J. Cosmol. Astropart. Phys. 03 (2020) 050.
[75] B. P. Abbott *et al.* (LIGO Scientific and Virgo Collaborations), *Tests of General Relativity with the Binary Black Hole Signals from the LIGO-Virgo Catalog GWTC-1*, Phys. Rev. D **100**, 104036 (2019).
[76] R. Abbott *et al.* (LIGO Scientific and Virgo Collaborations), *Tests of General Relativity with Binary Black Holes from the Second LIGO-Virgo Gravitational-Wave Transient Catalog*, Phys. Rev. D **103**, 122002 (2021).
[77] R. Abbott *et al.* (LIGO Scientific, Virgo, and KAGRA Collaborations), *Tests of General Relativity with GWTC-3*, arXiv:2112.06861.
[78] E. Berti, K. Yagi, H. Yang, and N. Yunes, *Extreme Gravity Tests with Gravitational Waves from Compact Binary Coalescences: (II) Ringdown*, Gen. Relativ. Gravit. **50**, 49 (2018).
[79] A. Bauswein and H. T. Janka, *Measuring Neutron-Star Properties via Gravitational Waves from Binary Mergers*, Phys. Rev. Lett. **108**, 011101 (2012).
[80] A. Bauswein, H. T. Janka, K. Hebeler, and A. Schwenk, *Equation-of-State Dependence of the Gravitational-Wave Signal from the Ring-Down Phase of Neutron-Star Mergers*, Phys. Rev. D **86**, 063001 (2012).
[81] K. Hotokezaka, K. Kiuchi, K. Kyutoku, T. Muranushi, Y.-i. Sekiguchi, M. Shibata, and K. Taniguchi, *Remnant Massive Neutron Stars of Binary Neutron Star Mergers: Evolution Process and Gravitational Waveform*, Phys. Rev. D **88**, 044026 (2013).
[82] K. Takami, L. Rezzolla, and L. Baiotti, *Constraining the Equation of State of Neutron Stars from Binary Mergers*, Phys. Rev. Lett. **113**, 091104 (2014).
[83] V. Paschalidis, *General Relativistic Simulations of Compact Binary Mergers as Engines for Short Gamma-Ray Bursts*, Classical Quantum Gravity **34**, 084002 (2017).
[84] B. D. Metzger, E. Quataert, and T. A. Thompson, *Short Duration Gamma-Ray Bursts with Extended Emission from Proto-Magnetar Spin-Down*, Mon. Not. R. Astron. Soc. **385**, 1455 (2008).
[85] N. Bucciantini, B. D. Metzger, T. A. Thompson, and E. Quataert, *Short GRBs with Extended Emission from Magnetar Birth: Jet Formation and Collimation*, Mon. Not. R. Astron. Soc. **419**, 1537 (2012).
[86] A. Bauswein, Niels-Uwe F. Bastian, D. B. Blaschke, K. Chatziioannou, J. A. Clark, T. Fischer, and M. Oertel, *Identifying a First-Order Phase Transition in Neutron Star Mergers through Gravitational Waves*, Phys. Rev. Lett. **122**, 061102 (2019).
[87] M. Breschi, S. Bernuzzi, D. Godzieba, A. Perego, and D. Radice, *Constraints on the Maximum Densities of Neutron Stars from Postmerger Gravitational Waves with Third-Generation Observations*, Phys. Rev. Lett. **128**, 161102 (2022).
[88] Y. Sugahara and H. Toki, *Relativistic Mean Field Theory for Unstable Nuclei with Nonlinear Sigma and Omega Terms*, Nucl. Phys. **A579**, 557 (1994).
[89] S. Typel, G. Ropke, T. Klahn, D. Blaschke, and H. H. Wolter, *Composition and Thermodynamics of Nuclear Matter with Light Clusters*, Phys. Rev. C **81**, 015803 (2010).
[90] A. W. Steiner, M. Hempel, and T. Fischer, *Core-Collapse Supernova Equations of State Based on Neutron Star Observations*, Astrophys. J. **774**, 17 (2013).
[91] P.-G. Reinhard and H. Flocard, *Nuclear Effective Forces and Isotope Shifts*, Nucl. Phys. **A584**, 467 (1995).
[92] A. Akmal, V. R. Pandharipande, and D. G. Ravenhall, *The Equation of State of Nucleon Matter and Neutron Star Structure*, Phys. Rev. C **58**, 1804 (1998).
[93] K. Takami, L. Rezzolla, and L. Baiotti, *Spectral Properties of the Post-Merger Gravitational-Wave Signal from Binary Neutron Stars*, Phys. Rev. D **91**, 064001 (2015).
[94] C. Palenzuela, S. L. Liebling, D. Neilsen, L. Lehner, O. L. Caballero, E. O'Connor, and M. Anderson, *Effects of the Microphysical Equation of State in the Mergers of Magnetized Neutron Stars with Neutrino Cooling*, Phys. Rev. D **92**, 044045 (2015).
[95] Y. Sekiguchi, K. Kiuchi, K. Kyutoku, and M. Shibata, *Effects of Hyperons in Binary Neutron Star Mergers*, Phys. Rev. Lett. **107**, 211101 (2011).
[96] N. Stergioulas, A. Bauswein, K. Zagkouris, and H.-T. Janka, *Gravitational Waves and Nonaxisymmetric Oscillation Modes in Mergers of Compact Object Binaries*, Mon. Not. R. Astron. Soc. **418**, 427 (2011).
[97] R. Abbott *et al.* (LIGO Scientific, Virgo, and KAGRA Collaborations), *The Population of Merging Compact Binaries Inferred Using Gravitational Waves through GWTC-3*, arXiv:2111.03634.
[98] T. Damour, A. Nagar, and L. Villain, *Measurability of the Tidal Polarizability of Neutron Stars in Late-Inspiral Gravitational-Wave Signals*, Phys. Rev. D **85**, 123007 (2012).
[99] H. Miao, H. Yang, and D. Martynov, *Towards the Design of Gravitational-Wave Detectors for Probing*

Neutron-Star Physics, Phys. Rev. D **98**, 044044 (2018).

[100] H. Yang, V. Paschalidis, K. Yagi, L. Lehner, F. Pretorius, and N. Yunes, *Gravitational Wave Spectroscopy of Binary Neutron Star Merger Remnants with Mode Stacking*, Phys. Rev. D **97**, 024049 (2018).

[101] W. E. East and L. Lehner, *Fate of a Neutron Star with an Endoparasitic Black Hole and Implications for Dark Matter*, Phys. Rev. D **100**, 124026 (2019).

[102] L. Barsotti, M. Evans, and P. Fritschel, *Alignment Sensing and Control in Advanced LIGO*, Classical Quantum Gravity **27**, 084026 (2010).